aerospace

MDPI

Article

Influence of Herringbone Grooves Inspired by Bird Feathers on Aerodynamics of Compressor Cascade under Different Reynolds Number Conditions

Shaobing Han [1,*], Zhijie Yang [1], Jingjun Zhong [2] and Yuying Yan [3]

[1] Naval Architecture and Ocean Engineering College, Dalian Maritime University, Dalian 116026, China; as1565581820@163.com
[2] Merchant Marine College, Shanghai Maritime University, Shanghai 201306, China; zhongjj@shmtu.edu.cn
[3] Faculty of Engineering, University of Nottingham, University Park, Nottingham NG7 2RD, UK; yuying.yan@nottingham.ac.uk
* Correspondence: hanbing2013@dlmu.edu.cn

Abstract: Nowadays, high aerodynamic load has made blade separation an issue for compact axial compressors under high-altitude low-Reynolds-number conditions. In this study, herringbone grooves inspired by bird feathers were applied to suppress the suction side separation and reduce loss. To study the effect of bio-inspired herringbone grooves on the aerodynamic performance of compressor cascades, a high subsonic compressor cascade was taken as the research object. Under the conditions of different Reynolds numbers, the effects of herringbone grooves of different depths on the flow separation were numerically studied. The research results show that at a high-Reynolds-number condition ($Re = 5.6 \times 10^5$), the sawtooth-shaped wake induced by herringbone grooves increases the turbulent mixing loss near the suction surface, and the blade performance deteriorates. At a low-Reynolds-number condition ($Re = 1.3 \times 10^5$), the span-wise secondary flow and micro-vortex structure induced by the herringbone grooves effectively suppress the laminar separation on the suction surface of the blade, and there is an optimal depth for the herringbone grooves that reduces the profile loss by 8.33% and increases the static pressure ratio by 0.55%. The selection principle of the optimal groove depth with the *Re* is discussed based on the research results under six low-Reynolds-number conditions.

Keywords: herringbone grooves; compressor cascade; Reynolds number; profile loss

check for updates

Citation: Han, S.; Yang, Z.; Zhong, J.; Yan, Y. Influence of Herringbone Grooves Inspired by Bird Feathers on Aerodynamics of Compressor Cascade under Different Reynolds Number Conditions. *Aerospace* **2024**, *11*, 626. https://doi.org/10.3390/aerospace11080626

Academic Editor: Christian Breitsamter

Received: 18 June 2024
Revised: 25 July 2024
Accepted: 29 July 2024
Published: 31 July 2024

Copyright: © 2024 by the authors. Licensee MDPI, Basel, Switzerland. This article is an open access article distributed under the terms and conditions of the Creative Commons Attribution (CC BY) license (https://creativecommons.org/licenses/by/4.0/).

1. Introduction

Microturbines have extensive application prospects in the field of unmanned aerial vehicles (UAVs) [1]. Their small size results in low-Reynolds-number working conditions, which is a typical characteristic that differentiates them from ordinary gas turbines. Under low-Reynolds-number conditions, the flow capacity and efficiency of the engine's main core components decrease, and the stable operating margin of the entire machine is reduced [2]. Therefore, the study and improvement of the influence of low-Reynolds-number conditions on the aerodynamic performance of core engine components has become a research hotspot. Current flow control methods mainly include active control methods that introduce external energy into the boundary layer [3,4] and passive control methods that modify the shape of the blades and end walls [5,6].

As a passive flow control method, biomimetic grooves have attracted the attention of researchers. The experimental studies of Bechert et al. [7] demonstrated that appropriately shaped longitudinal grooves can reduce pipe wall friction by 9.9%. Choi [8] investigated the effect of grooves on plate flow and found that the boundary layer characteristics of the grooved surface underwent significant changes. Miao et al. [9] conducted an experiment on engraving patterns on the surface of compressor blades and developed suitable

pattern forms that can significantly improve the critical Mach number, flow turning angle, and maximum static pressure ratio of the blade cascade. Zhao et al. [10] conducted an experimental study on three non-smooth blades with symmetric V-shaped grooves on a low-speed plane turbine cascade. The results showed that compared with the smooth blade cascade, the non-smooth blade cascade had a significantly reduced energy loss coefficient at the outlet and a more uniform outlet flow field. Ma et al. [11] experimentally investigated the influence of micro-grooved surfaces on the flow over an expansion-turning blade cascade and found that micro-grooved surfaces can suppress the development of the backflow boundary layer, reduce the span-wise flow of low-velocity fluid within the boundary layer, and weaken the interaction between the backflow boundary layer and the backflow corner vortex. Hergt et al. [12] experimentally investigated the effect of suction surface stream-wise grooves on the aerodynamic performance of a compressor cascade under two different incoming flow turbulence intensities. They found that the stream-wise grooves had a relatively small impact on the viscous losses of the blades. The large eddy simulation study conducted by Li [13] showed that micro-grooves can suppress the lateral pulsation of the turbulent boundary layer. The presence of the groove structure causes the turbulent vortices within the turbulent boundary layer to lift along the wall-normal direction, resulting in a reduced contact area between the turbulent vortex structure and the solid wall.

In recent years, researchers have combined the concept of biomimicry with grooved non-smooth surfaces, and a herringbone-shaped surface mimicking bird feathers has received attention. Compared with the longitudinal grooved surface, herringbone-shaped grooves have a specific angle to the mainstream direction, which induces different near-wall flow characteristics and boundary layer effects. Chen et al. [14] covered a section of the inner surface of a circular pipe with herringbone grooves and measured its flow loss. The experimental results showed that herringbone grooves with an included angle of 60° had the highest drag reduction rate, which could reach 21%, much higher than the traditional stream-wise grooved surface. Guo et al. [15] numerically investigated the control effect of herringbone grooves on laminar separation and found that separation was delayed at the groove divergence line and accelerated at the convergence line. Liu et al. [16] investigated the effect of herringbone groove geometric parameters on the profile loss of a conventional-loaded compressor blade cascade.

Synthesizing the current research, investigations on the application of herringbone grooves to a highly loaded compressor cascade need to be further conducted. The rules of their effect on the laminar separation bubble loss of blade cascades under different Re conditions and their mechanism of action remains unclear. Therefore, it is necessary to further explore the mechanism of the effect of herringbone grooves on the performance of highly loaded compressor cascades under different Re conditions.

2. Methodology

2.1. Research Object

The research object is a high subsonic compressor cascade with an NACA65-K48 airfoil profile, as shown in Figure 1. The specific geometric and aerodynamic parameters of the cascade are shown in Table 1.

Table 1. Geometry and aerodynamic parameters of cascade.

Parameters	Values
Chord, C/(mm)	40
Axial chord, Cz/(mm)	36.95
Span, H/(mm)	40
Pitch, t/(mm)	22
Stagger angle, φ/(°)	22.5
Design inlet angle, α/(°)	42
Design incidence, i/(°)	−6
Inlet Mach number, Ma_{in}	0.67

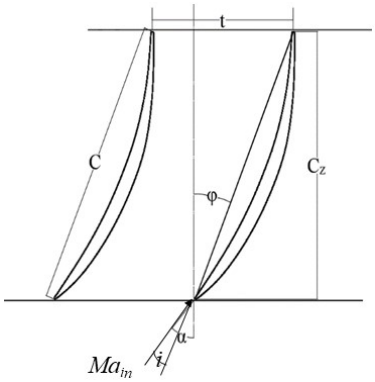


Figure 1. Schematic of blade profile.

Referring to the microstructure of the bird feathers shown in Figure 2, the suction surface herringbone grooves of the designed compressor blade are shown in Figure 3. The groove front is 0.2-chord lengths from the blade's leading edge, and the end is 0.6-chord lengths from the leading edge. To study the effect of herringbone grooves on the profile loss of the blade, the grooves are arranged in the middle area of the blade, which minimizes the influence of the end-wall corner loss. The groove cross-section is an inverted trapezoid, and the relevant geometric parameters are shown in Table 2.

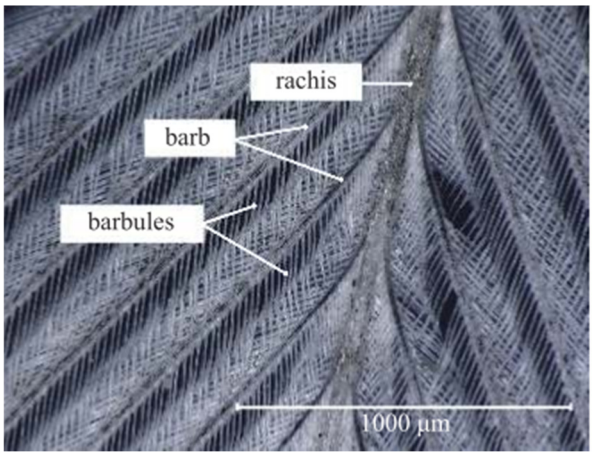
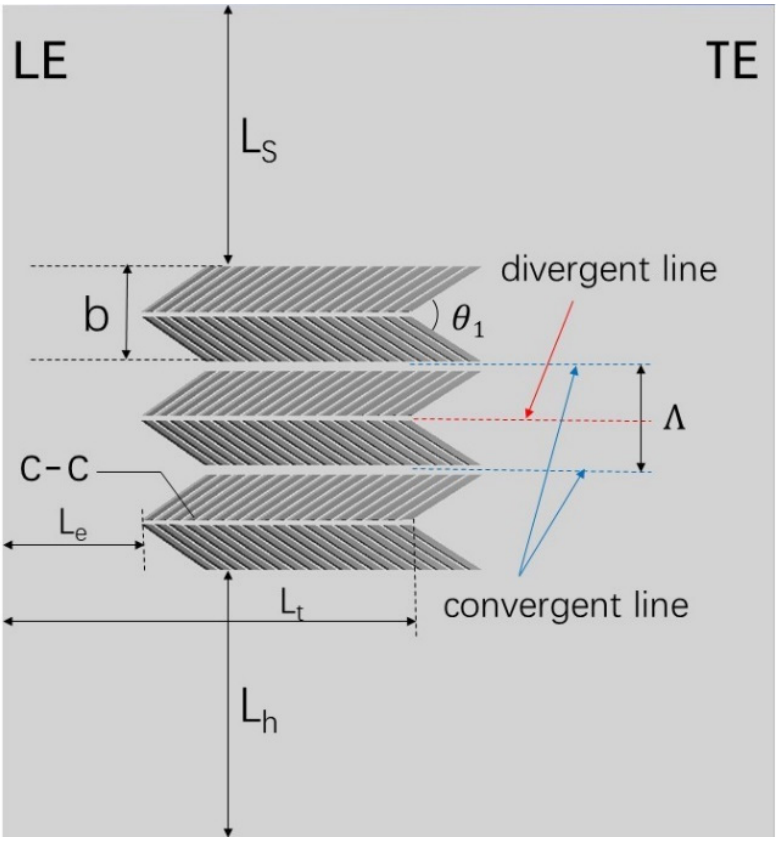


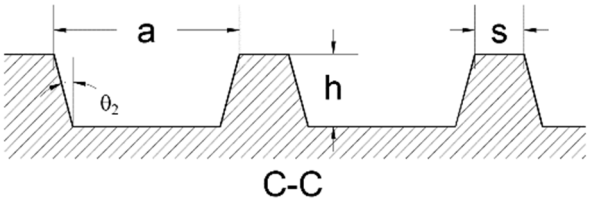
Figure 2. Microstructure of bird feathers [17].

Table 2. Geometric parameters of herringbone grooves.

Parameters	Values
L_s/(mm)	12.6
L_h/(mm)	12.6
L_e/(mm)	6.4
L_t/(mm)	21.6
θ_1/(°)	60
θ_2/(°)	10
b/(mm)	4.55
Λ/(mm)	5
a/(mm)	0.65
s/(mm)	0.2
h/(mm)	0.1, 0.2, 0.3, 0.4



(**a**)



(**b**)

Figure 3. Herringbone groove layout location and geometric parameters: (**a**) herringbone groove layout location; (**b**) cross-section parameters of grooves.

According to results in the literature [15], the groove depth is a key geometric parameter that affects the strength of the groove-induced vortex. This paper mainly performs calculations for four groove-depth schemes. The groove depth *h* is 0.1 mm, 0.2 mm, 0.3 mm, and 0.4 mm, respectively, denoted as Case 1–Case 4. The original blade cascade is denoted as Baseline.

2.2. Numerical Method

The three-dimensional steady RANS equation group is solved using ANSYS CFX 2020 software. The Shear Stress Transport turbulence model with the coupled γ-θ transition model is selected to close the equation group. The computational grid is divided into an "O4H"-type grid using NUMECA IGG. The inlet and outlet sections of the computational domain are located 2 chord lengths upstream and downstream of the blade leading and trailing edges, respectively. The thickness of the first layer of the near-wall grid is set to 1 μm, leading to a corresponding average y+ value on the wall equal to 0.25, thereby meeting the requirements of the SST turbulence model. First, grid independence verification is conducted on the Baseline case with different numbers of grids, and the specific results are shown in Figure 4. When the number of grids increases to 2.4 million, continuing to

increase the number of grids has little impact on the numerical simulation. Taking into account the time cost of numerical calculations, the number of grids selected is 2.4 million. Similar to the above approach, after grid independence verification, the number of grids for the blade schemes with herringbone grooves is 6.5 million to 7 million. The computational grid is shown in Figure 5.

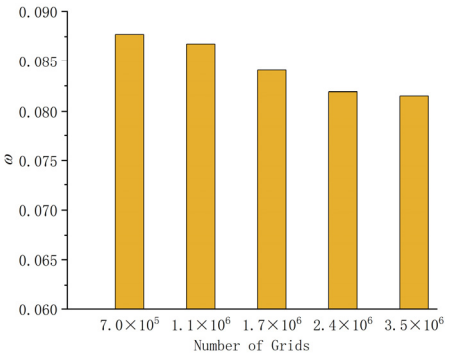


Figure 4. Grid number independence verification.

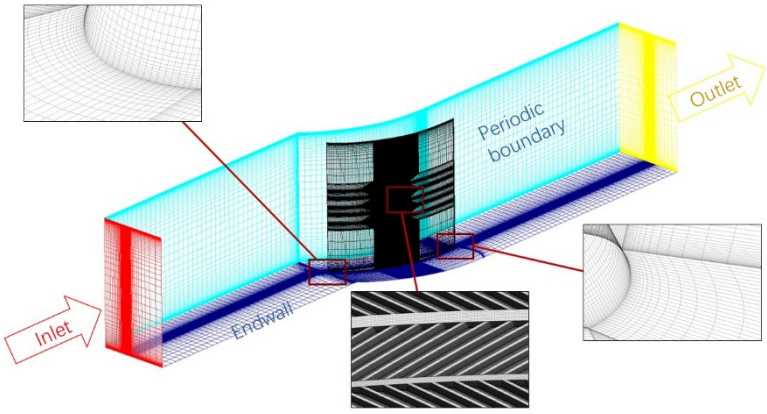


Figure 5. Computational grid and boundary conditions.

In terms of setting the calculation boundary conditions, the total pressure, total temperature, flow angle, and turbulence intensity are given at the inlet, and the average static pressure is given at the outlet. The blade surface and the upper- and lower-end walls are set as adiabatic no-slip walls, and the sides of the blade cascade channel are set as translational periodic boundary conditions along the span-wise direction. During the calculation, under the condition that the inlet Mach number is 0.67, the inlet total pressure and outlet static pressure are simultaneously adjusted to achieve different *Re*.

2.3. Numerical Reliability Verification

The experimental results of the literature [18] are used to verify the reliability of the numerical method used in this paper. The total pressure loss coefficient ω is defined as follows:

$$\omega = \frac{p_{in}^* - p^*}{p_{in}^* - p_{in}} \tag{1}$$

where p_{in}^* is the total pressure of the inlet; p^* is the local total pressure at the exit plane; and p_{in} is the static pressure of the inlet.

Figures 6 and 7 are the pitch-wise averaged total pressure loss coefficient and flow angle distributions along the blade height at the outlet section of the Baseline cascade, respectively. It can be seen from the figures that the overall trend of the total pressure loss coefficient and flow angle obtained by numerical simulation is in good agreement with

the experimental results. The calculated total pressure loss coefficient in the middle region of the blade is slightly smaller than the experimental value, and the flow angle is slightly larger than the experimental value. In other blade-height ranges, the numerical values and experimental values are the same. Therefore, it can be considered that the numerical method used in this paper is reliable.

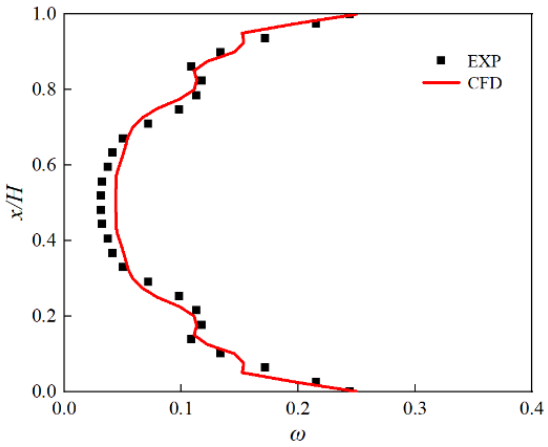


Figure 6. Span-wise distribution of pitch-wise averaged total pressure loss coefficient.

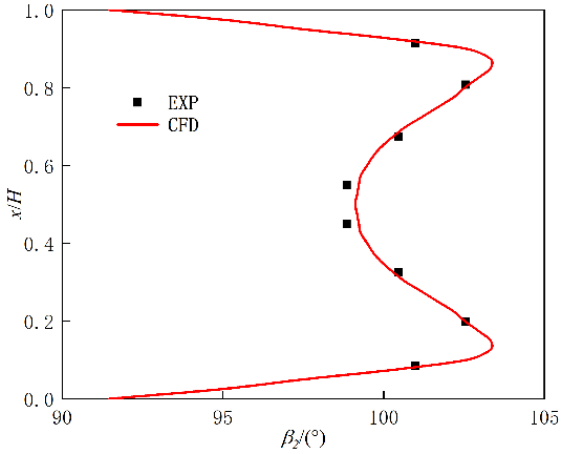


Figure 7. Span-wise distribution of pitch-wise averaged outlet flow angle.

3. Results and Discussion

3.1. Effect of Herringbone Grooves on Blade Performance at a High-Reynolds-Number Condition ($Re = 5.6 \times 10^5$)

Figure 8 shows the mass-averaged total pressure loss coefficient and static pressure ratio coefficient in the 35–65% blade-height range at the outlet section of the blade cascade at a high-Reynolds-number condition ($Re = 5.6 \times 10^5$), and the variation trend with the depth of the herringbone groove h. The static pressure ratio coefficient is defined as follows:

$$\pi = \frac{p}{p_{in}} \tag{2}$$

where p_{in} is the static pressure of the inlet; and p is the local static pressure at the exit plane.

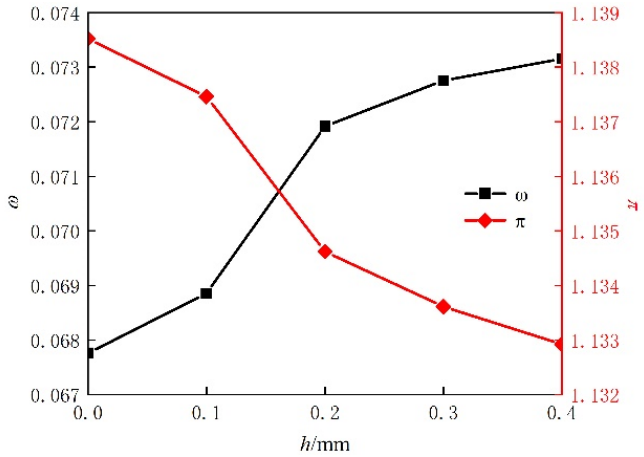


Figure 8. Comparison of the aerodynamic performance of different cases ($Re = 5.6 \times 10^5$).

It can be seen from Figure 8 that with the increase in the groove depth, the profile loss gradually increases, and the static pressure ratio coefficient of the blade cascade gradually decreases. The groove scheme of h = 0.1~0.4 mm increases the profile loss of the blade cascade by 1.61%, 6.14%, 7.38%, and 7.95%, respectively.

To quantitatively analyze the effect of herringbone grooves on the outlet loss of the blade cascade, Figure 9 shows the distribution of the total pressure loss averaged over the outlet section pitch along the blade height for the original blade cascade and the modified schemes. It can be observed from Figure 8 that all the groove-depth modified schemes reduce the total pressure loss in the 5~20% blade-height range to varying degrees, and the improvement effect of the blade cascade separation loss increases with the increase in the groove depth. Furthermore, the groove structure significantly increases the profile loss in the middle of the blade (35~65% blade-height range). When $h \geq 0.2$ mm, the total pressure loss in the middle of the modified blade cascade increases significantly compared to the original type, and the total pressure loss coefficient exhibits a monotonic increasing trend with the groove depth. Since this part of the loss is mainly composed of the profile loss, the increase in this part of the loss is the primary cause of the increase in the overall loss of the modified blade cascade.

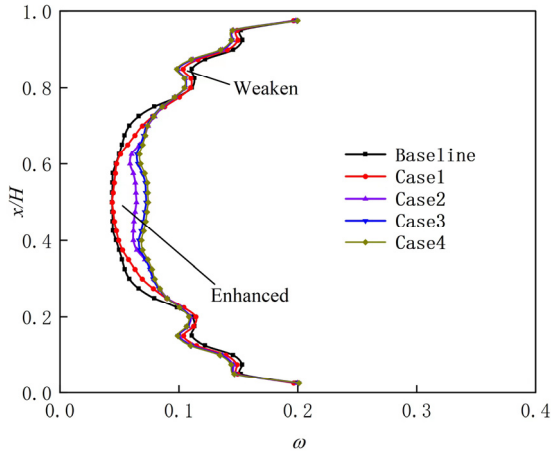


Figure 9. Span-wise distribution of pitch-wise averaged total pressure loss coefficient of different cases ($Re = 5.6 \times 10^5$).

To investigate the variation law of the total pressure loss in the blade cascade passage in detail, seven sections are intercepted along the axial direction, with each section located at 0% *Cz*, 20% *Cz*, 40% *Cz*, 60% *Cz*, 80% *Cz*, 100% *Cz*, and 120% *Cz* from the blade's leading edge, respectively, as depicted in Figure 10. After 60% of the axial chord length

in the original blade cascade passage, the low-energy fluid near the blade leading edge is primarily concentrated within the blade surface boundary layer. As the flow progresses downstream, the low-energy fluid begins to accumulate near the end-wall corner region, forming a high total pressure loss region, while the loss in the central portion of the blade is lower. In comparison to the original blade cascade, the upstream flow in the herringbone-groove blade cascade channel does not exhibit significant changes. Beyond 40% of the chord length, the herringbone groove, through its unique cross-arranged structure, induces the low-energy fluid within the suction surface boundary layer of the blade to redistribute, causing the blade surface boundary layer to exhibit a characteristic sawtooth pattern, as illustrated in Figure 10b. Under the influence of the groove, the fluid adjacent to the wall converges towards the groove convergence line, resulting in an increase in the boundary layer thickness at that location and a corresponding increase in the total pressure loss. Conversely, the fluid diverges towards both sides at the groove separation line, leading to a reduction in the boundary layer thickness and a decrease in the flow loss. Additionally, the placement of the grooves contributes to an increase in the blade surface boundary layer thickness near the trailing edge of the blade, and the high total pressure loss region in the central portion of the blade is noticeably larger compared to the original design.

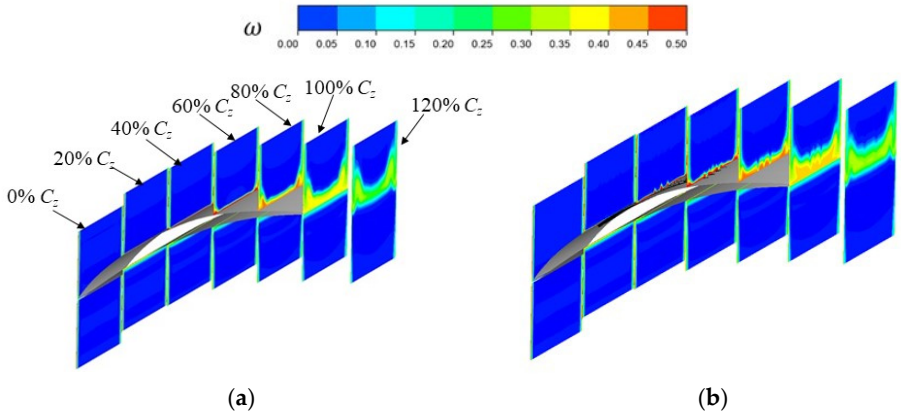


Figure 10. Contours of total pressure loss coefficient at different axial planes (Re = 5.6 × 10^5): (**a**) Baseline; (**b**) Case 4.

The arrangement of the herringbone grooves exerts an influence on the distribution of low-energy fluid within the blade surface boundary layer, as well as on the evolution and separation of the boundary layer. Figure 11 presents the distribution of the limiting streamlines on the suction surface and end wall for various schemes of the blade cascade. As depicted in Figure 11a, an extensive region of laminar separation bubbles emerges on the suction surface of the original blade, encompassing 80% of the blade-height range. Furthermore, a substantial region of corner separation flow is evident near the blade's trailing edge, indicating that corner separation loss constitutes the predominant portion of the total pressure loss in the highly loaded expansion blade cascade. Aside from the laminar separation bubble, the flow at the blade's mid-span is relatively well-behaved. In the herringbone-groove blade cascade, the groove structure exhibits a modest weakening effect on the separation bubble region and, to a certain extent, diminishes the area of the upper- and lower-end wall corner separation regions, thereby playing a role in suppressing end-separation. This is the underlying reason for the reduction in the total pressure loss coefficient within the 0~20% blade-height range at the outlet of the blade cascade for the groove scheme. When the groove depth is h = 0.4 mm, as shown in Figure 10b, a large region of backflow appears near the trailing edge at the blade's mid-span. In comparison to the ideal flow conditions in the middle of the original blade, the blade cascade flow under these conditions generates a considerable amount of flow loss in this region, leading to a noticeable increase in the high total pressure loss region at the outlet, accompanied by a significant expansion in the width of the wake region. Additionally, since the arrangement

of the groove structure is positioned at a distance from the end wall, its impact on the flow near the end-wall region is relatively minor. It can be inferred from these observations that under the condition of inlet $Re = 5.6 \times 10^5$, the arrangement of the herringbone grooves on the suction surface can exert a suppressive effect on the corner separation of the blade cascade to some extent, with a corresponding reduction in the total pressure loss near the end wall. However, under this Reynolds number condition, the groove significantly amplifies the mixing loss between the blade surface boundary layer and the mainstream region, thereby increasing the overall flow loss of the blade cascade.

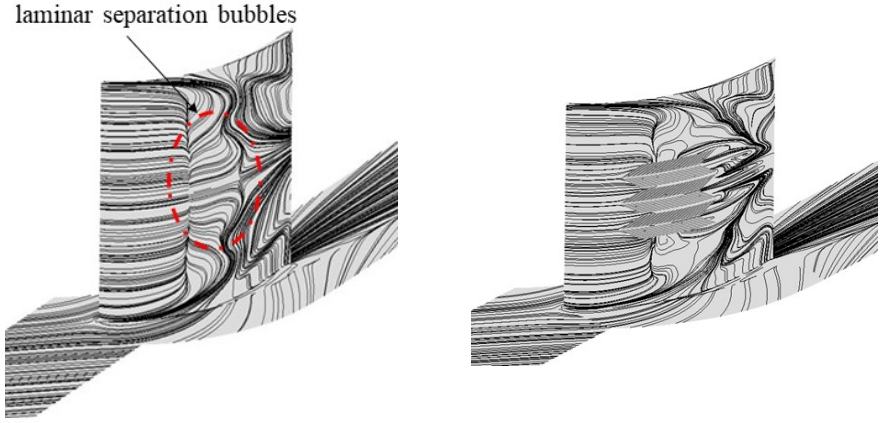


Figure 11. Surface limit streamlines on the suction side of the blade and the end wall ($Re = 5.6 \times 10^5$): (**a**) Baseline; (**b**) Case 4.

3.2. Effect of Herringbone Grooves on Blade Performance at a Low-Reynolds-Number Condition ($Re = 1.3 \times 10^5$)

To investigate the impact of herringbone grooves on blade performance at a low-Re condition, Figure 12 presents the variation trend of the mass-averaged total pressure loss coefficient and static pressure ratio coefficient within the 35~65% blade-height range at the outlet section of the blade cascade for $Re = 1.3 \times 10^5$. It can be observed that when the groove depth $h = 0.1$ mm, the profile loss exhibits a significant reduction, the blade's static pressure rise capability is effectively enhanced, and the blade's aerodynamic performance is notably improved. With a further increase in the groove depth h, the blade performance parameters are further enhanced, and when $h = 0.4$ mm, the profile loss is maximally reduced by 8.33%, while the static pressure ratio is increased by 0.55%. This demonstrates that under low-Reynolds-number conditions, herringbone grooves of an appropriate depth can effectively elevate the aerodynamic performance of compressor blades.

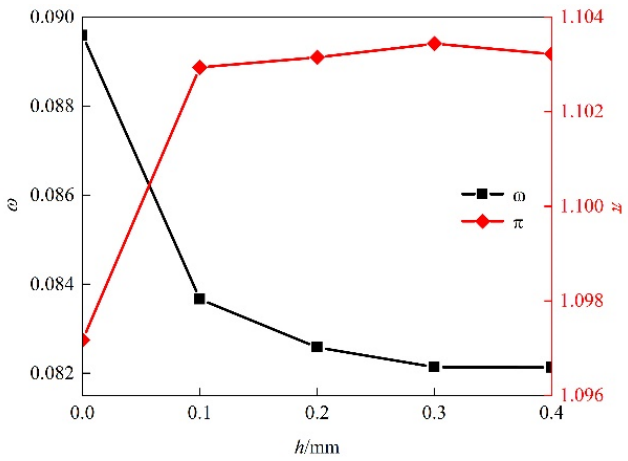


Figure 12. Comparison of the aerodynamic performance of different cases ($Re = 1.3 \times 10^5$).

Figure 13 presents the distribution comparison of the outlet section pitch-averaged total pressure loss coefficient along the blade height for different groove-depth schemes. It is evident that after the implementation of herringbone grooves, the total pressure loss coefficient within the 5~75% blade-height range at the outlet of the blade cascade is noticeably reduced, with the reduction being particularly significant at the middle span of the outlet of the blade cascade (i.e., the span-wise arrangement range of the herringbone grooves). In comparison to Case 1, the increase in groove depth h further reduces the loss at the middle span of the blade, while the variations among the Case 2–Case 4 schemes are relatively minor overall.

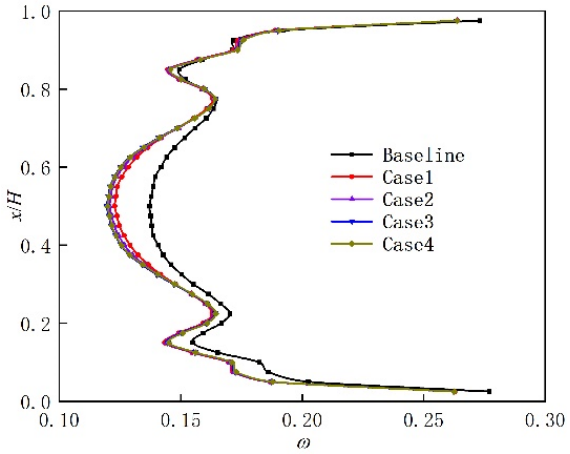


Figure 13. Span-wise distribution of pitch-wise averaged total pressure loss coefficient of different cases ($Re = 1.3 \times 10^5$).

To analyze the impact of herringbone grooves on the outlet wake of the blade cascade, Figure 14 presents a comparative distribution of the outlet section blade-height-averaged total pressure loss along the pitch for the original blade cascade and the modified scheme. It can be observed from the figure that all the groove schemes lead to a reduction in the high-loss value in the wake region of the blade, and the span-wise extent of the high-loss region along the wake is diminished. Comparing different groove schemes, the peak loss value of the wake decreases with an increase in the groove depth. Furthermore, it can be noted that the arrangement of the herringbone grooves primarily influences the wake loss distribution on the suction side of the blade, which is a consequence of its effective regulation of the near-wall flow characteristics on the suction side of the blade.

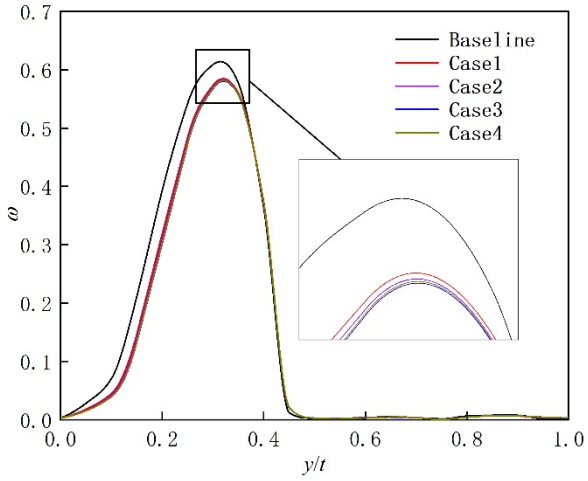


Figure 14. Pitch-wise distribution of span-wise averaged total pressure loss coefficient of different cases ($Re = 1.3 \times 10^5$).

Delving into the mechanism by which herringbone grooves reduce profile loss under low-Re conditions by combining the variations in the dissipation function distribution characteristics on the suction side of the blade in different blade cascade schemes, the dissipation function ψ is defined as follows:

$$\psi = \mu\left[\left(\frac{\partial v}{\partial x}+\frac{\partial u}{\partial y}\right)^2+\left(\frac{\partial w}{\partial x}+\frac{\partial u}{\partial z}\right)^2+\left(\frac{\partial v}{\partial z}+\frac{\partial w}{\partial y}\right)+\frac{2}{3}\mu\left[\left(\frac{\partial u}{\partial x}-\frac{\partial v}{\partial y}\right)^2+\left(\frac{\partial u}{\partial x}-\frac{\partial w}{\partial z}\right)^2+\left(\frac{\partial v}{\partial y}-\frac{\partial w}{\partial z}\right)^2\right]^2\right] + \frac{2}{3}\mu\left(\frac{\partial u}{\partial x}+\frac{\partial v}{\partial y}+\frac{\partial w}{\partial z}\right)^2 \quad (3)$$

where μ is the dynamic viscosity of the fluid; u, v, and w represent the velocity components of the fluid in the x, y, and z directions, respectively.

Figure 15 presents the dissipation function distribution contour plots for the original and grooved-blade cascades at various sections. To enhance the clarity of the analysis, the dissipation function is logarithmically transformed. The grooved scheme Case 4, which possesses superior geometric parameters, is selected for comparative analysis with the original blade cascade. Four sections are intercepted along the flow direction near the groove on the suction surface of the blade, located at 20% *Cz*, 40% *Cz*, 60% *Cz*, and 80% *Cz* from the blade's leading edge, respectively. As illustrated in Figure 15a, low-energy fluid accumulates within the laminar boundary layer of the original blade cascade, leading to elevated flow loss. The high-loss region primarily comprises the boundary layer separation loss and frictional loss. In contrast, for the grooved scheme, as depicted in Figure 15b, the distribution of the dissipation function near the wall exhibits notable changes. At the 40% *Cz* section, under the influence of the groove, the dissipation function exhibits a sawtooth-like distribution pattern: its value increases at the groove convergence line while it decreases at the groove separation line. This characteristic distribution becomes even more pronounced at the end of the herringbone groove (60% *Cz* section). The near-wall flow produces a distinct high-dissipation region downstream of the convergence line, accompanied by a corresponding increase in flow loss. Conversely, the flow loss downstream of the separation line is reduced, suggesting that the herringbone-shaped groove is capable of inducing span-wise micro-secondary flow within the boundary layer (as illustrated in Figure 16). Under the action of the groove, the intra-layer fluid gathers near the convergence line, resulting in an increase in the boundary layer thickness (from 0.8 mm to 1.2 mm) and an increase in flow loss. On the other hand, the fluid diverges to both sides at the separation line, the boundary layer thickness decreases, and the airflow loss decreases accordingly.

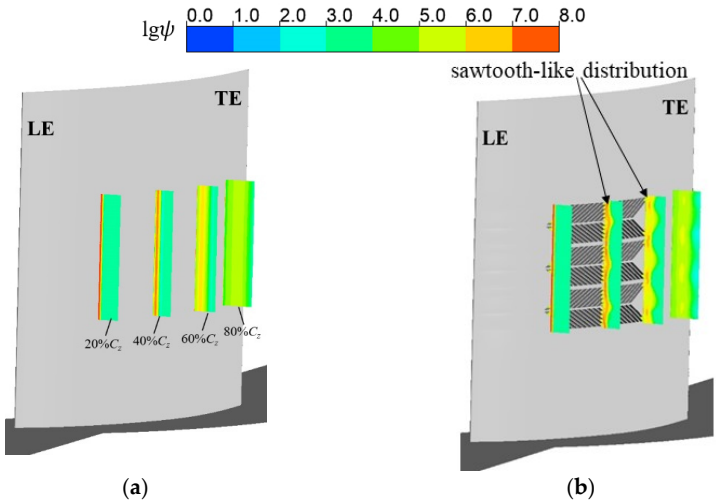


Figure 15. Contours of dissipation function on different axial planes (Re = 1.3 × 10^5): (**a**) Baseline; (**b**) Case 4.

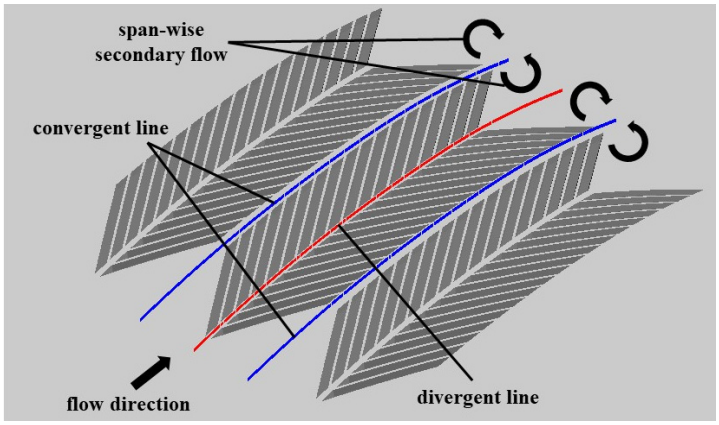


Figure 16. Schematic diagram of flow patterns near the herringbone grooves ($Re = 1.3 \times 10^5$).

Figure 17 presents the distribution of the turbulent kinetic energy on the blade's suction surface along the axial direction. It can be observed that the turbulent kinetic energy (TKE) level of the original blade cascade is relatively low from the leading edge to 0.4 *Cz*, indicating that the boundary layer in this region is in a laminar state. As the flow progresses downstream, the suction surface boundary layer undergoes laminar separation and subsequently transitions to turbulence. The turbulent kinetic energy level on the suction surface also rises continuously, reaching a maximum at the point of 0.6 *Cz*. Beyond this point, the turbulent kinetic energy level exhibits a reduction near the trailing edge due to the influence of the corner separation, which leads to the accumulation of low-energy fluid near the end region. In the case of the herringbone-groove blade cascade, the turbulent kinetic energy level within the range (0.3~0.7 *Cz*) where the herringbone groove is positioned on the suction surface of the blade is considerably elevated, and this increase is more pronounced with increasing groove depth. The rise in turbulent kinetic energy on the blade's suction surface suggests that the momentum exchange between the wall boundary layer fluid and the mainstream is intensified. The herringbone groove, on the one hand, induces a span-wise micro-secondary flow of the near-wall fluid, while on the other hand, it facilitates the mixing of the boundary layer fluid and the mainstream through the micro-vortex structures (as illustrated in Figure 18) within the groove, thereby enhancing the stream-wise momentum of the near-wall fluid and suppressing laminar separation on the suction surface of the blade.

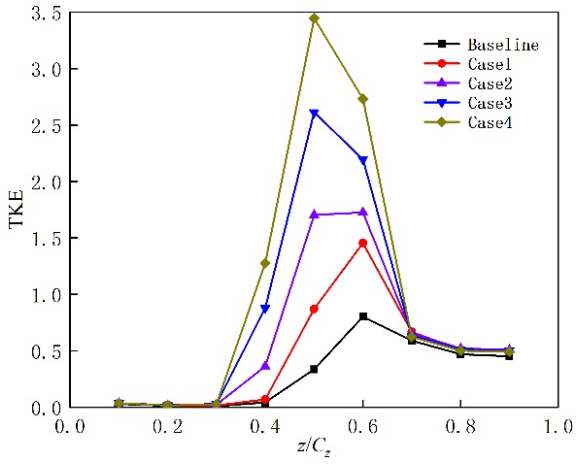


Figure 17. Axial distribution of TKE on the suction side of the blade ($Re = 1.3 \times 10^5$).

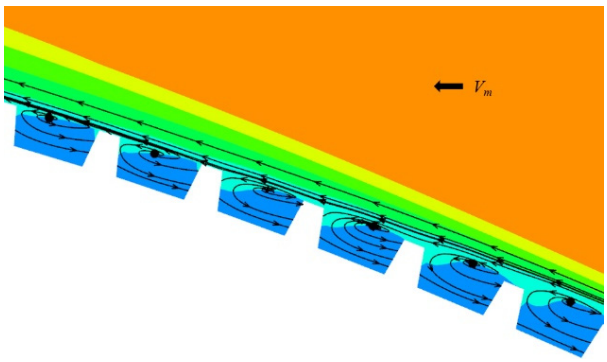


Figure 18. Streamline distribution inside the grooves ($Re = 1.3 \times 10^5$).

To visualize the alterations induced by the grooves on the boundary layer of the blade cascade, a comparative analysis is conducted on the velocity profiles of the blade suction surface boundary layer at 50% blade height for the grooved scheme and the original configuration. As depicted in Figure 19, two sets of monitoring points are selected on the suction surface, situated at 0.5 *Cz* and 0.7 *Cz*, respectively. This monitoring location corresponds to the end of the groove, which provides a favorable vantage point for examining the impact of the herringbone groove on the boundary layer. It can be observed that, owing to the groove's facilitation of mixing between the boundary layer fluid and the mainstream, the near-wall velocity distribution in the grooved scheme is more uniform. Consequently, the suction surface boundary layer of the blade exhibits enhanced resistance to separation. Additionally, the herringbone groove transforms the near-wall velocity at 0.7 *Cz* from a negative to a positive value, indicating that the herringbone groove suppresses the backflow resulting from laminar separation at this location.

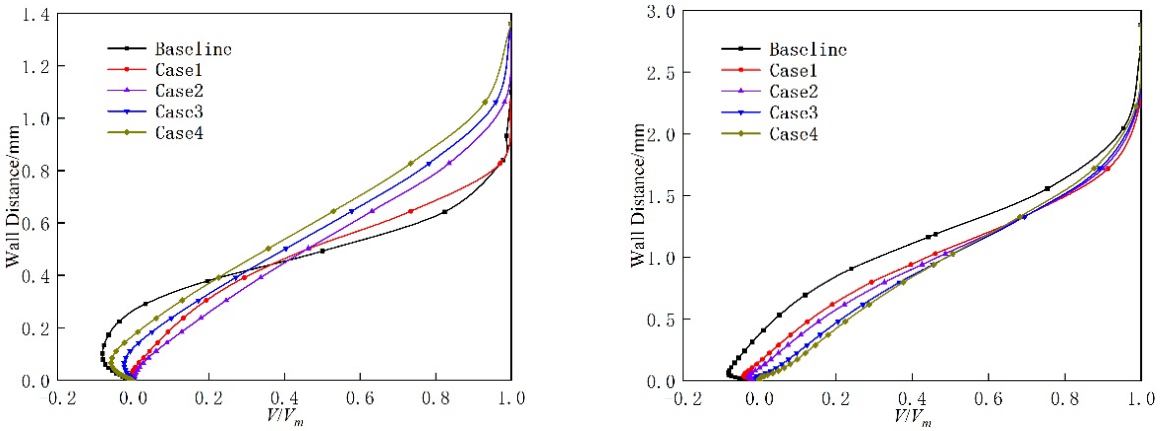


Figure 19. Velocity profiles on the suction side of the blade at different locations ($Re = 1.3 \times 10^5$): (**a**) 0.5 *Cz*; (**b**) 0.7 *Cz*.

3.3. Determining the Optimal Depth of Herringbone Grooves at Different Re Conditions

To investigate the optimal groove depth corresponding to the minimum profile loss in the herringbone-groove blade cascade at different Re conditions, Figures 20 and 21 present the relationship between the profile loss and the static pressure ratio as a function of the herringbone-groove depth for various *Re*. It is evident that at $Re = 1.3 \times 10^5$, the optimal groove depth is $h = 0.4$ mm. As *Re* increases, the optimal groove depth progressively decreases, reaching $h = 0.1$ mm at $Re = 2.5 \times 10^5$. Beyond this point, the groove depth $h = 0.1$ mm scheme consistently yields the lowest profile loss as *Re* continues to increase. Under the optimal groove depth, the static pressure ratio is enhanced across all six Reynolds-number conditions. Synthesizing the analysis, it can be concluded that a larger groove

depth exerts a more substantial influence on the suction surface flow field of the blade. Lower inlet Re values correspond to more severe laminar separation on the suction surface of the blade, necessitating a deeper herringbone groove to effectively regulate the boundary layer fluid on the blade's suction surface. This principle can serve as a guideline for the practical application of herringbone grooves in engineering.

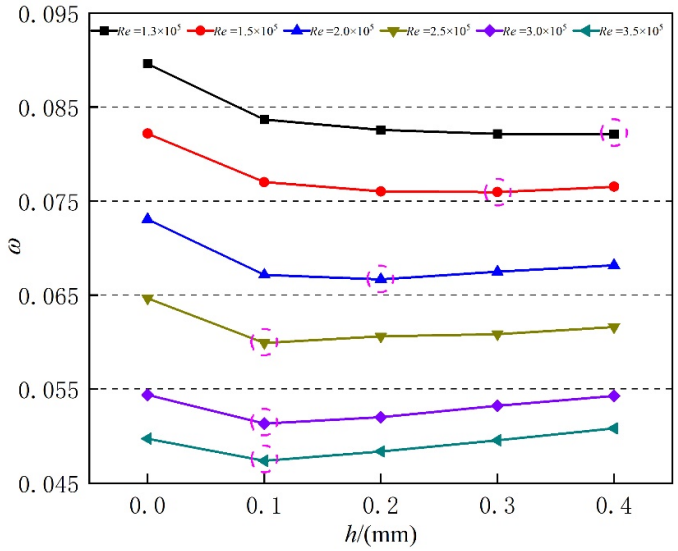


Figure 20. Profile loss varied with *h* at different *Re* conditions.

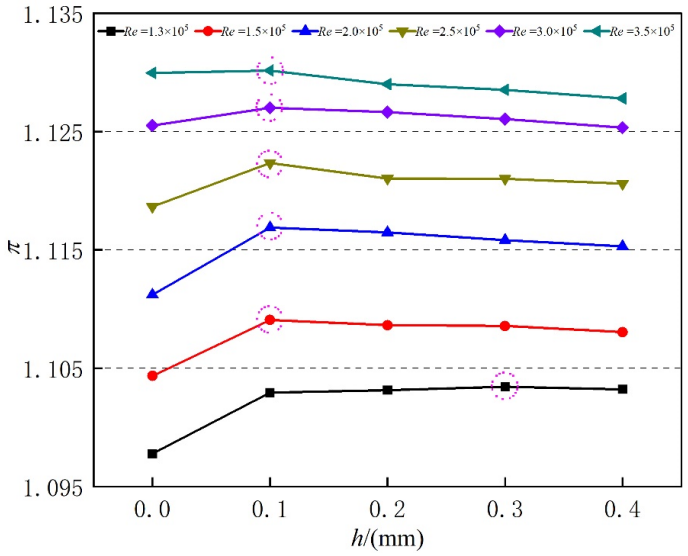


Figure 21. Static pressure ratio varied with *h* at different *Re* conditions.

4. Conclusions

Focusing on a highly loaded compressor blade cascade, this paper numerically investigates the influence of herringbone-groove depth on profile loss under different Re conditions and then concludes the design rules of herringbone grooves. The conclusions of this paper are as follows:

1. At a high-Reynolds-number condition ($Re = 5.6 \times 10^5$), the sawtooth-shaped wake induced by the herringbone groove increases the turbulent mixing loss near the suction surface, deteriorating blade performance. With increasing herringbone-groove depth, the extent of blade performance degradation becomes more pronounced;
2. At a low-Reynolds-number condition ($Re = 1.3 \times 10^5$), the herringbone groove produces a more uniform near-wall velocity distribution, effectively suppressing laminar

separation on the blade's suction surface. An optimal herringbone-groove depth exists, resulting in an 8.33% reduction in profile loss and a 0.55% improvement in static pressure ratio;

3. As a near-wall flow control technique, the herringbone groove operates by enhancing the mixing between the suction surface boundary layer fluid and the mainstream through the span-wise micro-secondary flow it induces and the micro-vortex structures within the groove;
4. In the *Re* range of 1.3×10^5 to 3.5×10^5, there exists an optimal groove depth h for each *Re* that minimizes the profile loss of the compressor blade, and the lower the blade inlet *Re*, the larger the optimal h value.

Author Contributions: Conceptualization, S.H.; methodology, Z.Y.; software, Z.Y.; validation, S.H., J.Z. and Y.Y.; formal analysis, Z.Y.; investigation, S.H.; resources, S.H.; data curation, Z.Y.; writing—original draft preparation, Z.Y. and S.H.; writing—review and editing, S.H. and Y.Y.; visualization, S.H.; supervision, S.H.; project administration, S.H.; funding acquisition, S.H. and J.Z. All authors have read and agreed to the published version of the manuscript.

Funding: This research was co-supported by the National Natural Science Foundation of China (52236005, 51406021), the Science Center for Gas Turbine Project (P2022-B-II-007-001). Also, the authors gratefully acknowledge financial support from the China Scholarship Council.

Data Availability Statement: The data presented in this study are available on request from the corresponding author.

Acknowledgments: The authors would like to acknowledge the first author's academic visit at the University of Nottingham during the academic year of 2023–2024.

Conflicts of Interest: The authors declare that they have no known competing financial interests or personal relationships that could have appeared to influence the work reported in this paper.

Nomenclature

Re	Reynolds number
C	chord
Cz	axial chord
H	span
t	pitch
φ	stagger angle
α	design inlet angle
i	design incidence
Ma_{in}	inlet Mach number
ω	total pressure loss coefficient
p^*_{in}	total pressure of the inlet
p^*	local total pressure
p_{in}	static pressure of the inlet
p	local static pressure
π	static pressure ratio coefficient
ψ	dissipation function
TKE	turbulent kinetic energy
V_m	mainflow velocity
h	groove height
a	groove width
s	groove spacing
β_2	outlet flow angle
x	span-wise direction
y	pitch-wise direction
z	axial direction
μ	dynamic viscosity

References

1. Hu, X. Development of high-altitude long endurance UAV propulsion technology. *Gas Turbine Exp. Res.* **2006**, *19*, 56–60.
2. Ling, D.; Wang, H.; Ma, C. Subsonic compressor plan cascade experiment at low Reynolds number. *Gas Turbine Exp. Res.* **2013**, *28*, 171–179.
3. List, J.; Byerley, A.; McLaughlin, T.; Van Dyken, R. Using plasma actuators flaps to control laminar separation on turbine blades in a linear cascade. In Proceedings of the 41st Aerospace Sciences Meeting and Exhibit, Reno, Australia, 6–9 January 2003.
4. Reijnen, D.P. Experimental Study of Boundary Layer Suction in a Transonic Compressor. Ph.D. Thesis, Massachusetts Institute of Technology, Cambridge, MA, USA, 1997.
5. Chen, Y.; Yang, L.; Zhong, J. Numerical study on endwall fence with varying geometrical parameters in a highly-loaded compressor cascade. *Aerosp. Sci. Technol.* **2019**, *94*, 105390. [CrossRef]
6. Nilavarasan, T.; Joshi, G.N.; Misra, A. Effect of microramps on flare-induced shock-boundary-layer interaction. *Aeronaut. J.* **2019**, *124*, 1–29. [CrossRef]
7. Bechert, D.W.; Bruse, M.; Hage, W.V.; Van der Hoeven, J.T.; Hoppe, G. Experiments on drag-reducing surfaces and their optimization with an adjustable geometry. *J. Fluid Mech.* **1997**, *338*, 59–87. [CrossRef]
8. Choi, K.S. Near-wall structure of a turbulent boundary layer with riblets. *J. Fluid Mech.* **1989**, *208*, 417–458. [CrossRef]
9. Miao, R.; Wang, L. Effect of hub treatment on performance of an axial flow compressor. *J. Aerosp. Power* **1991**, *6*, 13–16.
10. Wen, J.; Zhao, G. An experimental study on effect of unsmoothed blade on cascade exit loss distribution. *J. Aerosp. Power* **2000**, *15*, 44–46.
11. Tian, Q.; Ma, H.; Wu, H.; Gao, L. Effects of a kind of groove surface on the surface flow field of a compressor cascade. *J. Eng. Thermophys.* **2006**, *27*, 177–180.
12. Hergt, A.; Hage, W.; Grund, S.; Steinert, W.; Terhorst, M.; Schongen, F.; Wilke, Y. Riblet application in compressors: Toward efficient blade design. *J. Turbomach.* **2015**, *137*, 111006. [CrossRef]
13. Li, Z.; Jin, Y.; Du, J.; Zhang, H.; Nie, C. Physical mechanisms investigation of sharkskin-inspired compressor cascade based on large eddy simulations. *J. Turbomach.* **2021**, *143*, 061005. [CrossRef]
14. Chen, H.; Rao, F.; Shang, X.; Zhang, D.; Hagiwara, I. Flow over bio-inspired 3d herringbone wall riblets. *Exp. Fluids* **2014**, *55*, 1698. [CrossRef]
15. Guo, T.; Zhong, S.; Craft, T. Control of laminar flow separation over a backward-facing rounded ramp with c-d riblets—The effects of riblet height, spacing and yaw angle. *Int. J. Heat Fluid Flow* **2020**, *85*, 108629. [CrossRef]
16. Liu, Q.; Zhong, S.; Li, L. Effects of bio-inspired micro-scale surface patterns on the profile losses in a linear cascade. *J. Turbomach.* **2019**, *141*, 121006. [CrossRef]
17. Wu, K.; Ye, Z.; Ye, K.; Hong, Z. Mechanical characteristics of the deformation of bird feathers in airflow. *Chin. J. Theor. Appl. Mech.* **2023**, *55*, 874–884.
18. Hergt, A.; Meyer, R.; Liesner, K.; Nicke, E. A new approach for compressor endwall contouring. In Proceedings of the ASME 2011 Turbo Expo: Turbine Technical Conference and Exposition. Volume 7: Turbomachinery, Parts A, B, and C, Vancouver, BC, Canada, 6–10 June 2011; ASME: New York, NY, USA, 2011; ASMEGT2011-54679.

Disclaimer/Publisher's Note: The statements, opinions and data contained in all publications are solely those of the individual author(s) and contributor(s) and not of MDPI and/or the editor(s). MDPI and/or the editor(s) disclaim responsibility for any injury to people or property resulting from any ideas, methods, instructions or products referred to in the content.